Nanoscale

PAPER

View Article Online
View Journal | View Issue

Cite this: *Nanoscale*, 2015, **7**, 10078

Hydrogen gas sensor based on metal oxide nanoparticles decorated graphene transistor†

Zhangyuan Zhang,[a] Xuming Zou,[a] Lei Xu,[a] Lei Liao,*[a] Wei Liu,[a] Johnny Ho,[b] Xiangheng Xiao,*[a] Changzhong Jiang[a] and Jinchai Li[a]

Received 26th March 2015,
Accepted 1st May 2015

DOI: 10.1039/c5nr01924a

www.rsc.org/nanoscale

In this work, in order to enhance the performance of graphene gas sensors, graphene and metal oxide nanoparticles (NPs) are combined to be utilized for high selectivity and fast response gas detection. Whether at the relatively optimal temperature or even room temperature, our gas sensors based on graphene transistors, decorated with SnO_2 NPs, exhibit fast response and short recovery times (~1 seconds) at 50 °C when the hydrogen concentration is 100 ppm. Specifically, X-ray photoelectron spectroscopy and conductive atomic force microscopy are employed to explore the interface properties between graphene and SnO_2 NPs. Through the complimentary characterization, a mechanism based on charge transfer and band alignment is elucidated to explain the physical originality of these graphene gas sensors: high carrier mobility of graphene and small energy barrier between graphene and SnO_2 NPs have ensured a fast response and a high sensitivity and selectivity of the devices. Generally, these gas sensors will facilitate the rapid development of next-generation hydrogen gas detection.

1. Introduction

Gas sensors play an increasingly important role in our modern society, particularly for industrial production and public security.[1–4] Among many different gases, the rapid detection of dangerous gases such as hydrogen is technologically essential as these gases are typically colorless, odorless, and highly explosive in a wide range. In this regard, various kinds of gas sensors have been extensively explored and developed, including solid electrolyte gas sensors,[5] metal oxide gas sensors,[6–8] electrochemical gas sensors[9] and graphene-based gas sensors.[10–12] It is noted that metal oxides represent an appealing class of materials owing to their high sensitivity to most gases, low cost, and simple fabrication techniques.[4] As early as 1962, gas sensors based on metal oxide were demonstrated by Seiyama.[12] Later, different metal oxides involving CeO_2, ZnO, SnO_2, and CuO were reported as the active materials for hydrogen detection.[3,6,7,13] The working principle of such gas sensors is based on the conductivity change when metal oxides are surrounded by hydrogen.[14] Moreover, the recent advent of nanotechnology provides a further impetus to the development of metal oxide-based gas sensors,[3,6–8] and the previously dominant metal oxide thin films have now been substituted by nanowires,[3,6] nanoflakes,[15] or nanoparticles,[16,17] since the unique characteristic of larger surface-to-volume ratio in these nanostructures would greatly improve the sensor response speed accordingly. For instance, Yamazoe showed that the metal oxide particles with a smaller crystallite size gave considerable improvement to the sensor performance.[18] Even so, there are still some unresolved issues for these metal oxide gas sensors such as the relatively high operating temperatures (usually over 200 °C) as well as the long response and recovery times.[19] The high operating temperatures would impose a substantial safety risk during the gas detection and put a noteworthy restriction on practical utilization of these sensors due to their corresponding energy consumption, being inconsistent with the green energy concept. Also, a fast response speed is necessary such that the users can receive an advance warning when the dangerous gas is detected. In addition, depletion layers generally appear around the metal oxide NPs which will induce a large energy barrier for electrons transferring from grain to grain, and in some cases, the depletion layer may even slow down the response of the devices.[20] All these problems indicate that the metal oxide-based gas sensors need further optimization in order to meet the current needs.

At the same time, graphene-based gas sensors are also widely investigated.[21,22] Since its discovery in 2004, graphene has attracted significant attention in many technological aspects because of its excellent properties: large surface area,

[a]*Department of Physics and Key Laboratory of Artificial Micro- and Nano-structures of Ministry of Education, Wuhan University, Wuhan 430072, China. E-mail: liaolei@whu.edu.cn, xxh@whu.edu.cn*
[b]*Department of Physics and Materials Science, City University of Hong Kong, Hong Kong SAR, China*

†Electronic supplementary information (ESI) available. See DOI: 10.1039/c5nr01924a

high mobility, chemical stability, *etc.*[21–23] It is hoped that the excellent device performance of graphene can significantly overcome the shortcomings of existing gas sensors. Till now, several types of graphene materials have been utilized in the hydrogen gas sensors, including exfoliated graphene, chemical vapor deposition (CVD) graphene and reduced graphene oxide (RGO).[10,11,22] However, for the lack of dangling bonds, few molecules are adsorbed on the surface of exfoliated graphene and CVD graphene.[24] As to the RGO, its advantages mainly include a number of dangling bonds and low-cost synthesis on a large scale,[25,26] but the relatively low mobility would limit its performance in rapid detection.[26]

Herein, we present a facile and rational design to achieve fast-response hydrogen gas sensors by combining graphene with metal oxide NPs. Through such an approach, metal oxide NPs act as active elements for gas detection while graphene is used for the subsequent electron transfer facilitation for performance enhancement. The key is that once hydrogen is detected, electrons acquired from NPs could transfer to the underlying graphene quickly. But, the Schottky barrier originated from different work functions of metal oxide NPs and graphene would lead to an obstacle for electron transfer as soon as they are in contact, while the work function of metal oxide NPs matches that of graphene, and this Schottky barrier would become insignificant. This way, it will be easy for electrons to pass through the barrier, and hence will lead to the high sensitivity and fast response in gas sensing. In this work, three typical metal oxide NPs (SnO_2, CuO and ZnO) are employed as the representative hydrogen gas active materials. Notably, it is confirmed that our scheme can reasonably modulate the Schottky barrier to achieve high sensitivity and fast response for hydrogen gas detection even at room temperature (RT). Besides, sensor arrays built on the CVD graphene with consistent and excellent performance further indicate their technological potency for large-scale applications. At the end, through the detailed characterization, we discuss and verify the physical mechanism of our gas sensors which illustrates the operability at RT and the capability of rapid response in hydrogen detection.

2. Results and discussion

2.1. Device schematic and electrical properties

Graphene was obtained by the mechanical exfoliation method and then was transferred to the SiO_2/Si substrate. The samples were heated to 200 °C under air for 10 minutes to ensure the formation of metal oxide NPs after the metal film deposition. The source and drain electrodes were defined by electron beam lithography (JEOL 6510 with NPGS System), followed by the 10 nm/40 nm Cr/Au deposition and lift-off process. The channel length was 3 μm. The overall design concept is illustrated in Fig. 1. In detail, the single layer exfoliated high quality graphene demonstrates the superior carrier mobility; however, due to the absence of dangling bonds, these devices exhibit no obvious sensitivity to the hydrogen gas (Fig. 1a).[24] For example, in Fig. S1,† transfer curves of the representative graphene FET are given under different types of atmosphere (air, H_2 and vacuum); it is obvious that no significant change is observed when the external environment changes. After decorated with metal oxide NPs, the graphene FET can provide abundant dangling bonds *via* the NPs. With the extraordinary surface-to-volume ratio, these metal oxide NPs on graphene can now well connect with gas molecules in the surrounding and then interact with them efficiently owing to the grain boundaries and unsaturated bonds (Fig. 1b); as a result, the graphene FET would yield excellent sensitivity to hydrogen gas, which will be discussed thoroughly in the following session. Basic electrical properties of both graphene FET and graphene FETs decorated with metal oxide NPs are shown in Fig. 1c. It is clear that the undecorated FET has a symmetrical transfer curve while the transfer curves of decorated FETs are asymmetric. We have also found that there is a significant reduction in the channel current after the deposition of metal oxide NPs. This current degradation may be attributed to the charged impurity scattering associated with the metal oxide layer. Similar impact of the oxide environment on electrical properties of graphene devices have been observed previously.[27,28] More importantly, as seen in scanning electron microscopy (SEM) image of our gas sensor (Fig. 1c, inset), the graphene sheet covered with metal oxide NPs is open-and-shut together with source and drain electrodes. In any case, the decorated graphene with the robust framework here still maintains its excellent performance.

2.2 Morphology characterization

In our devices, dispersive NPs are important for the gas detection in which they are responsible for yielding a fast response and high gas sensitivity as compared with the conventional sensors. The appropriate spacing among NPs (*i.e.* suitable particle distribution) ensures that hydrogen molecules can be adsorbed, thereby transferring electrons well to NPs, moreover the high surface-to-volume ratio of NPs would further enhance the performance in gas detection.[17] SEM (Hitachi S-4800) was performed to survey the surface morphology of gas sensors after the deposition of metal films followed by oxidation procedures under air. As illustrated in Fig. 2a–c, there is a highly visible boundary between the region with and without graphene. It is clearly observed that NPs are distributed uniformly on the graphene sheet and the spacing among NPs on graphene is larger than that on the SiO_2/Si substrate with respect to all kinds of metal oxide NPs. Atomic force microscopy (AFM, Bruker MultiMode 8) was also completed to meticulously study the surface topography on a small scale (Fig. 2a–c inset). In the insets, SnO_2 NPs seem to be more compact than ZnO NPs without losing much gap, which results in having more gas molecules adsorbed on SnO_2 NPs, and hence yield better performance in gas detection. For CuO NPs, the particle size is bigger than that of SnO_2 and ZnO NPs. In order to accurately observe and verify the differences in the distribution of these three particle types, the detailed particle size and height profile are assessed and given in Fig. 2d–f, with the black lines

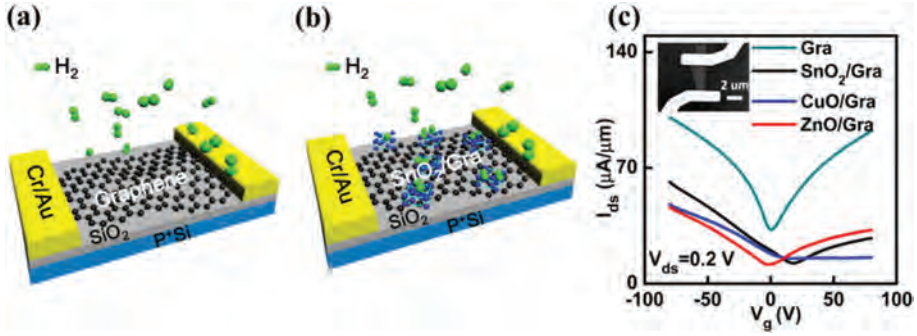

Fig. 1 (a) The schematic of graphene transistor without obvious sensitivity to hydrogen. (b) The schematic of graphene FET decorated by metal oxide NPs with obvious sensitivity to hydrogen. (c) The electrical characteristics of graphene FET and graphene transistors decorated with different metal oxide NPs. The inset is the top view SEM image of the decorated graphene gas sensor.

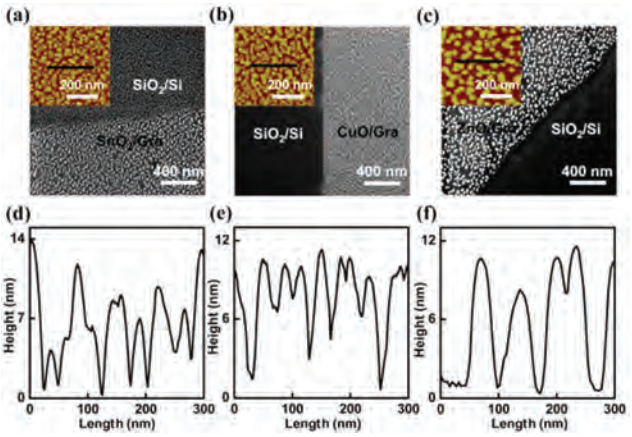

Fig. 2 Surface morphology after the different metal oxide NPs deposition: (a) SnO_2, (b) CuO, and (c) ZnO. The particle size or height profile of different decoration: (d) SnO_2, (e) CuO, and (f) ZnO, with the lateral measured range of 300 nm indicated in the black colored lines in the insets of a–c.

in Fig. 2a–c insets indicating the corresponding measurement position. After annealing, the metal films (about 2 nm in the nominal thickness) become metal oxide NPs due to crystallization and aggregation. SnO_2 NPs are distributed uniformly and densely while ZnO NPs also have an even distribution with a larger spacing. On the other hand, the spacing is smaller among CuO NPs (Fig. 2e). The large area AFM characterization is well performed indicating the same consistent trend and depicted in ESI Fig. S2.† From the morphology characterization, SnO_2 NPs are considered to have more advantages in gas sensing among the three types of metal oxide NPs.

2.3. Electrical characterization

In order to fully understand the sensor operation, the working phenomenon of our gas sensors based on metal oxide must be assessed and described. It is well-known that oxidizing (reducing) gases can be typically used as the electron acceptor (donor) and thus change the conductance of graphene FETs decorated with metal oxide NPs. When an oxidizing gas (*e.g.*, O_2) is introduced to the sensor, the following reaction will be triggered:

$$O_2 + e^- \rightarrow 2O^- \quad (1)$$

Here, O_2 serves as charge accepting molecules and acquires electrons from the surface of metal oxide NPs, leading to a reduction of electron concentration and then lowering the conductance of the graphene FET accordingly. Conversely, if the sensor is exposed to reducing gas (*e.g.*, H_2), the following reaction will occur:

$$H_2 + O^- \rightarrow H_2O + e^- \quad (2)$$

In this case, H_2 will react with the adsorbed oxygen ions on the surface of metal oxide NPs, and thus the electron concentration of graphene FET increases and enlarges the channel current. Hence, the graphene FET output current can act as the gas sensor output signal in the presence of different types of target gas atmospheres.[29,30]

The electrical characterization of the fabricated devices were characterized by Agilent 4155C semiconductor parameter analyzer with the Lake Shore TTPX Probe Station. Fig. 3a–c give the transfer curves of graphene FETs decorated with SnO_2, CuO, ZnO NPs, respectively. The metal films are all 2 nm in thickness before annealing. In Fig. 3a, the graphene FET decorated with SnO_2 NPs shows an excellent current modulation to the hydrogen gas, particularly in the region of positive gate bias (*i.e.* n-type branch). Again, when the gas sensor is exposed to hydrogen, the reaction of eqn (2) would be triggered. The electrons released by oxygen ions are then transferred to the underlying graphene channel such that the electron concentration is enlarged and the channel output current is increased accordingly. In other words, electrons are the majority carriers when graphene FETs operate at the n-type branch and the channel output current would become larger due to additional electrons released from oxygen ions. In the region of negative gate bias (*i.e.* p-type branch), it displays a small decrease in the current, which can be explained by the fact that the electrons released by oxygen ions cannot participate in the charge trans-

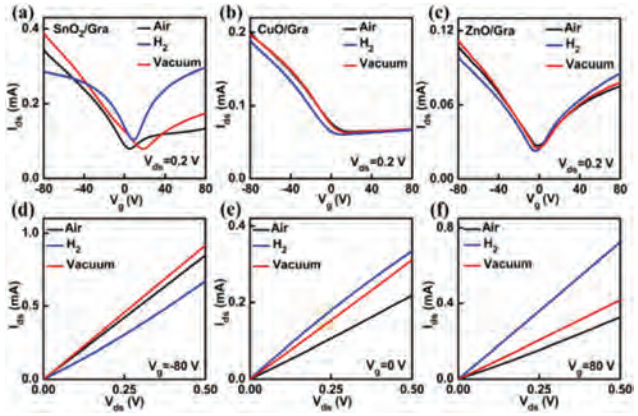

Fig. 3 I_{ds}–V_g curves of graphene transistors decorated with different metal oxide NPs: (a) SnO_2, (b) CuO, (c) ZnO. Corresponding I_{ds}–V_{ds} characteristics of the graphene transistor decorated by SnO_2 NPs: (d) V_g = −80 V, (e) V_g = 0 V, (f) V_g = 80 V. All tests are carried out under different conditions: air, H_2 and vacuum.

fer process where the holes are the majority carriers there. In Fig. 3b and c, this phenomenon is consistent and can be observed again. Among different types of NPs, the graphene FET decorated with SnO_2 NPs demonstrates the best sensitivity to hydrogen with a large current modulation at the n-type branch. Moreover, gas sensors decorated with SnO_2 NPs shows the good adsorption/desorption characteristics: after measurement and hydrogen is pumped out, the current reverts back to its baseline quickly. For the cases of CuO and ZnO NPs, no significant change in transfer behaviors (*i.e.* I_{ds}–V_g) suggests that they are quite insensitive to the hydrogen gas here. In Fig. 3d–f, a series of output behaviors (*i.e.* I_{ds}–V_{ds}) are given based on Fig. 3a. It is clear that there is a good match between I_{ds}–V_{ds} curves and I_{ds}–V_g curves with Fig. 3d corresponding to Fig. 3a when the back gate bias is fixed at −80 V. Fig. 3e and f are achieved in a similar way. Actually, we have also tried different metal oxide NPs in different thickness for exploring the best performance of our gas sensors. Fig. S3† shows the transfer curves of graphene FETs decorated with SnO_2, CuO, ZnO NPs of different thickness (1 and 3 nm thick metal films before annealing). From the comprehensive and systematic data, we find that the graphene FETs decorated with SnO_2 NPs (2 nm thick Sn film in the nominal thickness before annealing) show the largest current modulation to hydrogen.

In addition, gas response to three kinds of reducing gas was tested in this study to illustrate the selectivity of the graphene FET decorated with SnO_2, such as CO, NO, H_2. As shown in Fig. S4,† the channel current has no remarkable change when the gas sensor is surrounded by CO and NO and it is obvious that the decorated graphene FET shows a high sensitivity to H_2 in the n-type branch. So, we have obtained a desired gas sensor which has an ideal selectivity to H_2. The selectivity of the sensor can be explained by several factors such as electron affinity, catalytic efficiency, and adsorption properties. Obviously, if the electron affinity of target gas molecules is smaller, the energy required for gas sensing reaction will reduce and the sensitivity to this gas should be higher. Similarly, when the catalytic efficiency of surface oxygen is higher and the amount of gas adsorption on the sensing material is larger, the decorated graphene FET also shows a higher sensitivity to the target gas.[14,31,32] All these suggest that SnO_2 NPs can serve as a good gas sensing medium for hydrogen gas detection with the assistance of graphene.

2.4 Hydrogen sensing response

Sensitivity is an important parameter for high performance gas sensors and the detailed sensitivity study of our sensors will be discussed in the following section. The sensitivity test is conducted in a closed environment. Here, the sensitivity is defined as $S = I_g/I_a$, where I_g and I_a are the output currents acquired in the target gas and in the air stream, respectively. For conventional gas sensors based on metal oxide films, the operating temperatures may be up to 400 °C (usually higher than 200 °C).[19] Fig. 4a gives the relationship between the sensor sensitivity and operating temperature. Obviously, the relationship between gas sensitivity and operating temperature presents an ascending and then descending trend when the concentration of H_2 is fixed at 10 ppm in air. This phenomenon may be attributed to several reasons: first, a thin layer of adsorbed water molecules due to the humidity is likely to exist and cover the SnO_2 NPs surface and, to a certain extent, hinder the reaction between hydrogen gas molecules and oxygen ions.[33] Subsequently, raising the temperature within a certain range can help release the adsorbed humidity and thus enhance the response to H_2. Next, the reaction aimed at transferring electrons to graphene FETs may become more active at a relatively higher temperature, and hence improving the sensitivity of the gas sensor. Finally, the number of adsorbed oxygen ions on SnO_2 NPs would decrease to some extent when the temperature is rising.[34] This way, the electron transfer between hydrogen gas molecules and SnO_2 NPs would become inactive as the number of adsorbed oxygen ions decreases; therefore, the sensitivity of graphene FETs decorated with SnO_2 NPs will get degraded gradually. According to Fig. 4a, we believe that 50 °C is a relatively optimal temperature considering the parameter of sensitivity. Fig. 4b plots the real-time dynamic response of the SnO_2/graphene FET gas sensor exposed to H_2/air mixed gas at V_{ds} = 1 V and V_g = 80 V. The dynamic response to H_2 was conducted in a home-made gas sensing system based on Agilent 2902 source meter. Five successive ON/OFF cycles are successfully achieved corresponding to five different H_2 concentrations ranging from 1 ppm to 100 ppm, respectively. Importantly, the sensing behavior is reproducible, and as expected, increasing H_2 concentration leads to an increasing output current which subsequently enhances the sensitivity. It should be highlighted that the efficient detection of hydrogen concentrations down to 1 ppm indicates that our sensor is very suitable for perceiving H_2 at low levels.

Furthermore, the corresponding dynamic response in 100 ppm H_2 is also depicted in Fig. 4c. The largest sensitivity

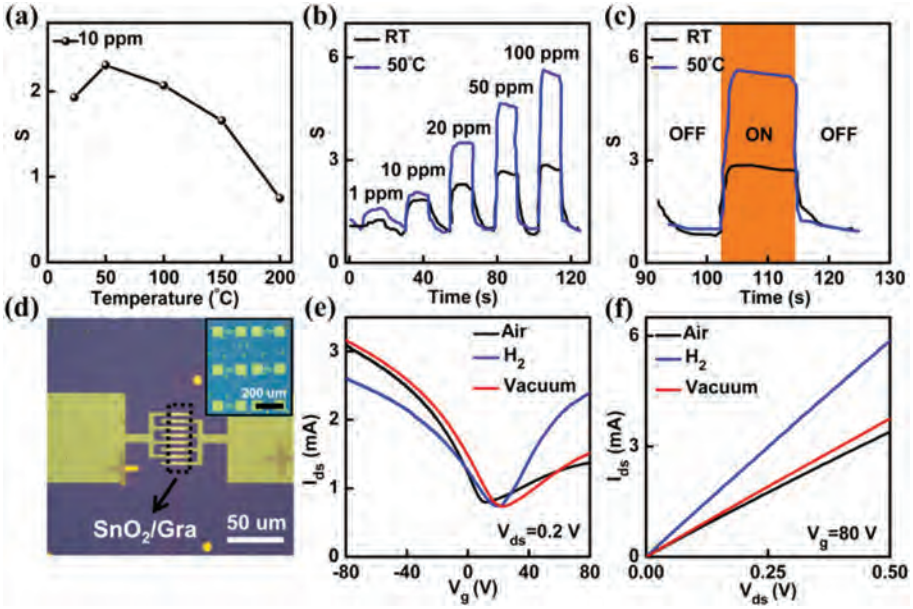

Fig. 4 (a) The sensitivity of the gas sensor decorated with SnO_2 NPs at various temperatures. (b) Real-time dynamic response of gas sensors decorated with SnO_2 NPs exposed to different H_2 concentrations at different operation temperatures. (c) The response and recovery times of the sensor exposed to the 100 ppm H_2 concentration. (d) Top view optical images of the gas sensor arrays. The graphene used here is grown from the CVD method. (e–f) Corresponding I_{ds}–V_g and I_{ds}–V_{ds} curves of the fabricated gas sensor arrays at room temperature.

of nearly 6 is observed when the temperature is 50 °C (~3 at RT), in which it is a respectable value due to the efficient electron transfer between SnO_2 NPs and graphene. Other important parameters including response and recovery times are also investigated. The response time is defined as the time needed for the current to increase by 63.2% from its base line in air to the maximum value in 100 ppm H_2, and the recovery time is the time required for the current to decrease by 63.2% from the maximum value in 100 ppm H_2 to the base value in air.[35] In our work, the response and recovery times are, respectively, determined as 1.1 s and 1.1 s (1.2 s and 1.6 s at RT). The response and recovery times obtained at 50 °C are both slightly shorter than those at RT, which is probably due to the faster processing rate at the higher temperature. Explicitly, the sensing process involves both the diffusion of H_2 and the redox reaction,[36] where the rapid response here indicates that the diffusion and redox reaction processes can be quickly completed in our devices. Compared to other gas sensors whose response time need a few minutes, our gas sensors based on graphene transistors decorated with SnO_2 NP make an encouraging progress.[1,2,16]

In order to study the practicability of our design concept for large-scale applications, CVD graphene is employed for fabricating this new kind of gas sensor (Fig. 4d). Regarding the detailed fabrication processes, there are some differences that the CVD graphene has to be patterned into neat strips with photolithography followed by O_2 plasma etching before the SnO_2 NPs deposition. Then, interdigital electrodes are defined on top of the graphene strips,[37] with the top view of devices illustrated in Fig. 4d. The inset shows the corresponding 3 × 2 arrays. The electrical characterization have been performed and presented in Fig. 4e and f; like those in Fig. 3a–f, the gas sensor arrays based on CVD graphene demonstrate excellent properties consistent with those shown by gas sensors using exfoliated graphene. The excellent performance of our devices suggests a great potential for industrial utilizations where the rapid detection at low temperature and low H_2 concentration is required.

2.5 Physical mechanism

Moreover, we have utilized systematic methods in order to investigate the physical mechanism of our high-performance gas sensors. Notably, all graphene samples studied here are synthesized with the CVD method. In previous statements of about the sensor operation (*i.e.* working phenomenon), we believe that the excellent sensor performance of SnO_2 decorated graphene FETs is rooted in the superior matching of energy barrier between graphene and metal oxide NPs when they are in contact. Therefore, conductive atomic force microscopy (CAFM) is employed to explore the carrier transport between SnO_2/Graphene (SnO_2/Gra). In Fig. 5a, two images are acquired with the left one reflecting the topographic information of graphene surface decorated with SnO_2 NPs, while the right one revealing the conductivity difference on the same graphene surface. In other words, all these yield the spatial mapping of the energy barrier height difference on the decorated graphene surface.[38] From Fig. 5a, we can clearly see that the larger current passes through the region where there are voids (marked by black circles), and hence the barrier is smaller. Then, in order to compare the barrier

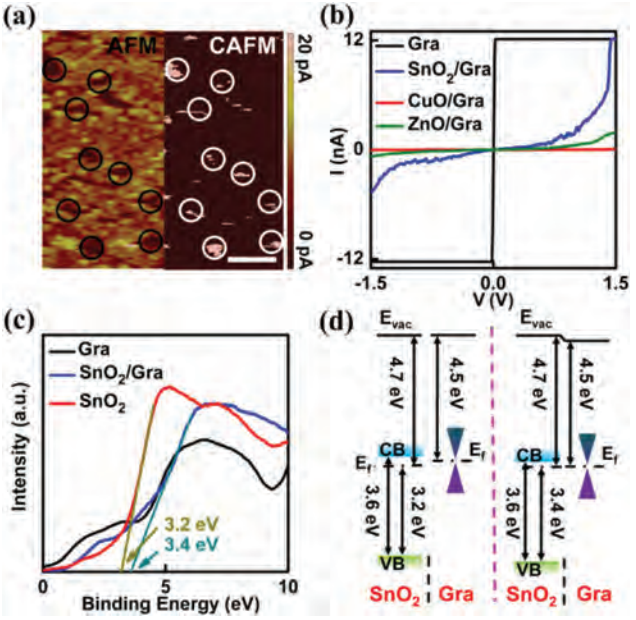

Fig. 5 (a) The CAFM current mapping obtained with the 10 mV tip bias and the scan size of 500 × 250 nm. The scale bar is 100 nm. (b) *I–V* characterization of a series of samples: graphene, SnO_2/Gra, CuO/Gra and ZnO/Gra. (c) Valence band spectra of different samples: graphene, SnO_2/Gra and SnO_2. (d) Band diagrams of the SnO_2/Gra near Fermi level: before and after the SnO_2 NPs deposition.

heights between graphene and different NPs (*i.e.* SnO_2, CuO and ZnO), *I–V* characterization is performed and shown in Fig. 5b. Each curve in Fig. 5b is achieved with the scan probe staying on one nanoparticle under the CAFM mode. From the obtained results, the barrier height among all NPs can be compared indirectly through the current: it gives the minimum barrier for the SnO_2/Gra contact since the corresponding current yields the maximum value there. On the other hand, the valence band spectrum of SnO_2/Gra interface is also surveyed by X-ray photoelectron spectroscopy (Thermo ESCALAB-250) as illustrated in Fig. 5c. Meanwhile, we also confirm that the Sn metal is completely oxidized after annealing, and the data is shown in ESI Fig. S5.† In particular, valence band spectra mainly show the information of electronic states near the Fermi level.[39] The change of valence band maximum before and after the SnO_2 NP deposition can be contrasted concisely. The energy difference between the Fermi level and the valence band maximum is 3.2 eV before the SnO_2 NP deposition, and then it becomes 3.4 eV after the SnO_2 NP deposition. For a good understanding of the valence band maximum change, the energy band diagram is schematically shown in Fig. 5c. The band gap of SnO_2 NPs is invariant such that the Fermi level shift would lead to the valence band maximum change. Comparing the work functions of graphene and SnO_2 NPs, it can be seen that the former one is smaller and the electrons can flow easily to SnO_2 NPs from graphene, resulting in the Fermi level shift after the SnO_2 NP deposition. After the Fermi level is aligned, the Schottky barrier between graphene and SnO_2 NPs is only 0.2 eV without considering other factors. In operation, the electrons can now pass through the barrier efficiently at the n-type branch. The same methods are also employed to analyze the CuO/Gra and ZnO/Gra contact, the characterization results are presented in Fig. S6.† From the band diagrams of CuO/Gra and ZnO/Gra interfaces, the energy barriers of CuO/Gra and ZnO/Gra interfaces are about 0.9 and 0.8 eV, respectively, which are much larger than that of SnO_2/Gra interface. Moreover, CuO is a p-type semiconductor; therefore, the graphene FETs decorated with CuO NPs show minimum sensitivity to hydrogen. In any case, benefitting from such a small barrier, we can obtain a fast response and high sensitivity in our SnO_2 decorated graphene gas sensors among three kinds of NPs.

3. Conclusion

In summary, we have fabricated a new type of gas sensor based on graphene transistors decorated with SnO_2 NPs. The new gas sensors can detect low-level H_2 at around room temperature. Importantly, the gas sensor exhibits a fast response time of 1.1 s and a high selectivity to hydrogen with a simple but reliable fabrication process. In addition, gas sensor arrays built on the CVD grown graphene are also developed with the consistent and excellent sensor performance. The CAFM and valence band characteristics of the SnO_2/Gra interface further illustrate and confirm that the small energy barrier plays a key role in the fast-response gas detection. Besides, uniformly dispersed metal oxide NPs together with high-mobility graphene also offer effective assistance for hydrogen gas sensing. As a result, all the excellent performance illustrates the bright prospects of our new approach in the development of next-generation efficient hydrogen gas detection.

Acknowledgements

We acknowledge the 973 grant of MOST (no. 2011CB932700 and 2013CBA01604), MOE (20120141110054), and NSFC grant (61222402, 61376085 and 61474084), Fundamental Research Funds for the Central Universities (no. 2042015kf0184) and the key grant of National Laboratory of Infrared Physics in Shanghai Institute of Technical Physics.

Notes and references

1 T. Wagner, S. Haffer, C. Weinberger, D. Klaus and M. Tiemann, *Chem. Soc. Rev.*, 2013, **42**, 4036–4053.
2 M. R. Mohammadi and D. J. Fray, *Sens. Actuators, B*, 2009, **141**, 76–84.
3 L. Liao, H. B. Lu, J. C. Li, C. Liu, D. J. Fu and Y. L. Liu, *Appl. Phys. Lett.*, 2007, **91**, 173110.
4 J. S. Lee, O. S. Kwon, S. J. Park, E. Y. Park, S. A. You, H. Yoon and J. Jang, *ACS Nano*, 2011, **5**, 7992–8001.

5 N. Miura, M. Nakatou and S. Zhuiykov, *Sens. Actuators, B*, 2003, **93**, 221–228.
6 L. Liao, H. X. Mai, Q. Yuan, H. B. Lu, J. C. Li, C. Liu, C. H. Yan, Z. X. Shen and T. Yu, *J. Phys. Chem. C*, 2008, **112**, 9061–9065.
7 A. Khanna, R. Kumar and S. S. Bhatti, *Appl. Phys. Lett.*, 2003, **82**, 4388–4390.
8 J. Yi, J. M. Lee and W. I. Park, *Sens. Actuators, B*, 2011, **155**, 264–269.
9 W. Weppner, *Sens. Actuators*, 1987, **12**, 107–119.
10 H. Y. Jeong, D.-S. Lee, C. Hong Kyw, D. H. Lee, K. Ji-Eun, J. Yong Lee, W. J. Lee, K. Sang Ouk and C. Sung-Yool, *Appl. Phys. Lett.*, 2010, **96**, 213105.
11 C. Soldano, A. Mahmood and E. Dujardin, *Carbon*, 2010, **48**, 2127–2150.
12 T. Seiyama, A. Kato, K. Fujiishi and M. Nagatani, *Anal. Chem.*, 1962, **34**, 1502–1503.
13 P. A. Russo, N. Donato, S. G. Leonardi, S. Baek, D. E. Conte, G. Neri and N. Pinna, *Angew. Chem., Int. Ed.*, 2012, **51**, 11053–11057.
14 G. Korotcenkov, *Mater. Sci. Eng., B*, 2007, **139**, 1–23.
15 M. Chen, Z. Wang, D. Han, F. Gu and G. Guo, *J. Phys. Chem. C*, 2011, **115**, 12763–12773.
16 E. R. Leite, I. T. Weber, E. Longo and J. A. Varela, *Adv. Mater.*, 2000, **12**, 965–968.
17 M. P. Prahalad, E. C. Richard and R. Z. Michael, *Nanotechnology*, 2006, **17**, 3786–3790.
18 N. Yamazoe, *Sens. Actuators, B*, 1991, **5**, 7–19.
19 Q. Wan, Q. H. Li, Y. J. Chen, T. H. Wang, X. L. He, J. P. Li and C. L. Lin, *Appl. Phys. Lett.*, 2004, **84**, 3654–3656.
20 A. Rothschild and Y. Komem, *J. Appl. Phys.*, 2004, **95**, 6374–6380.
21 Y. W. Zhu, S. Murali, W. W. Cai, X. S. Li, J. W. Suk, J. R. Potts and R. S. Ruoff, *Adv. Mater.*, 2010, **22**, 3906–3924.
22 U. Lange, T. Hirsch, V. M. Mirsky and O. S. Wolfbeis, *Electrochim. Acta*, 2011, **56**, 3707–3712.
23 Y. B. Zhang, Y. W. Tan, H. L. Stormer and P. Kim, *Nature*, 2005, **438**, 201–204.
24 S. Basu and P. Bhattacharyya, *Sens. Actuators, B*, 2012, **173**, 1–21.
25 A. Wei, J. Wang, Q. Long, X. Liu, X. Li, X. Dong and W. Huang, *Mater. Res. Bull.*, 2011, **46**, 2131–2134.
26 Y. H. Ding, P. Zhang, Q. Zhuo, H. M. Ren, Z. M. Yang and Y. Jiang, *Nanotechnology*, 2011, **22**, 215601.
27 Y.-M. Lin, K. A. Jenkins, A. Valdes-Garcia, J. P. Small, D. B. Farmer and P. Avouris, *Nano Lett.*, 2008, **9**, 422–426.
28 C. R. Dean, A. F. Young, I. Meric, C. Lee, L. Wang, S. Sorgenfrei, K. Watanabe, T. Taniguchi, P. Kim, K. L. Shepard and J. Hone, *Nat. Nanotechnol.*, 2010, **5**, 722–726.
29 C. Wang, L. Yin, L. Zhang, D. Xiang and R. Gao, *Sensors*, 2010, **10**, 2088–2106.
30 N. Bârsan and U. Weimar, *J. Phys.: Condens. Matter*, 2003, **15**, R813–R839.
31 Z. Wen and L. Tian-mo, *Physica B*, 2010, **405**, 1345–1348.
32 S. Kanan, O. El-Kadri, I. Abu-Yousef and M. Kanan, *Sensors*, 2009, **9**, 8158–8196.
33 R. K. Sharma, M. C. Bhatnagar and G. L. Sharma, *Sens. Actuators, B*, 1998, **46**, 194–201.
34 S. T. Shishiyanu, T. S. Shishiyanu and O. I. Lupan, *Sens. Actuators, B*, 2005, **107**, 379–386.
35 G. Lu, L. E. Ocola and J. Chen, *Adv. Mater.*, 2009, **21**, 2487–2491.
36 G. Korotcenkov, M. Ivanov, I. Blinov and J. R. Stetter, *Thin Solid Films*, 2007, **515**, 3987–3996.
37 J. Li, Y. Lu, Q. Ye, M. Cinke, J. Han and M. Meyyappan, *Nano Lett.*, 2003, **3**, 929–933.
38 I. C. Infante, F. Sanchez, V. Laukhin, A. Perez del Pino, J. Fontcuberta, K. Bouzehouane, S. Fusil and A. Barthelemy, *Appl. Phys. Lett.*, 2006, **89**, 172506.
39 M. T. Greiner, M. G. Helander, W.-M. Tang, Z.-B. Wang, J. Qiu and Z.-H. Lu, *Nat. Mater.*, 2012, **11**, 76–81.

